

# Regulating bimetallic active centers for exploring the structure-activity relationship upon high-performance photocatalytic nitrogen reduction

**Wensheng Zhang**

Guangzhou University

**Guoliang Pan**

Guangzhou University

**Dongfang Han**

Guangzhou University

**Tianren Liu**

Guangzhou University

**Weiqliang**

Guangzhou University

**Dongxue Han** (✉ [dxhan@gzhu.edu.cn](mailto:dxhan@gzhu.edu.cn))

Guangzhou University

**Mengjiao Dai**

Changchun Institute of Applied Chemistry, Chinese Academy of Sciences

**Haijiao Xie**

Hangzhou Yanqu Information Technology Co., Ltd.

**Dongdong Qin**

Guangzhou University

**Li Niu** (✉ [lniu@gzhu.edu.cn](mailto:lniu@gzhu.edu.cn))

Guangzhou University

---

## Research Article

**Keywords:** Photocatalytic nitrogen reduction reaction, Bimetallic Ti-Pd active centers, N<sub>2</sub>-bridging strategy, Structure-activity relationship, Side-on adsorption configuration

**Posted Date:** May 3rd, 2022

**DOI:** <https://doi.org/10.21203/rs.3.rs-1614980/v1>

**License:**  This work is licensed under a Creative Commons Attribution 4.0 International License.

[Read Full License](#)

# Abstract

Photocatalytic ammonia ( $\text{NH}_3$ ) synthesis from  $\text{N}_2$  is a strategy conducive to carbon neutrality because it avoids high energy consumption and high carbon emission process in the industrial synthesis of  $\text{NH}_3$ . However, the structure-activity relationship of bimetallic active centers in heterogeneous catalysts is still dimness for high-performance photocatalytic nitrogen reduction reaction (pNRR). Here, a rational  $\text{N}_2$ -bridging strategy for heterogeneously pNRR has been expanded through regulating bimetallic Ti-Pd active centers at  $\text{TiO}_2$  (101)/Pd (111) interface and the structure-activity correlation during the pNRR was explored. The side-on adsorption with “\*N  $\equiv$  N\*” configuration (\*presents the adsorption site) on Ti-Pd centers induces a considerable polarization and potent activation of  $\text{N}_2$ , enabling to achieve an impressive rate of  $\text{NH}_3$  production ( $635.73 \mu\text{g g}_{\text{cat}}^{-1} \text{h}^{-1}$ ) on the optimal se-Pd/m- $\text{TiO}_2$  NRs (2.71%). More importantly, nearly  $\sim 92.37\%$  of initial activity could be retained following 8 successive reaction rounds. Further mechanism studies revealed that the side-on bridging mode of  $\text{N}_2$  with bimetallic Ti-Pd centers possesses an ultra-high adsorption energy, which can effectively weaken the triple bond of  $\text{N}_2$  and reduce the activation energy barrier of pNRR process. This study provides insights into the electronic structure regulation of bimetallic active centers and structure-property relationship at the atomic level.

## Introduction

In recent years, the main consensus on tackling global climate changes is carbon neutrality. Nowadays, the vital shackle of carbon neutrality is the industrial synthesis of ( $\text{NH}_3$ ), which consumes 1%-3% of the global energy each year and emits 3% of global  $\text{CO}_2$ <sup>1,2</sup>. Photocatalytic synthesis of  $\text{NH}_3$  holds a promising perspective for the conversion of nitrogen ( $\text{N}_2$ ) to  $\text{NH}_3$  through solar-to-chemical energy with low energy consumption and zero-carbon emission. As a consequence of exceptionally robust  $\text{N} \equiv \text{N}$  triple bonds of  $\text{N}_2$  molecules by the bond energy of  $941 \text{ kJ}\cdot\text{mol}^{-1}$ , effective activation of  $\text{N}_2$  molecules over catalysts is typically considered to impede  $\text{N}_2$  reduction<sup>3,4</sup>. Numerous photocatalytic  $\text{N}_2$  fixation catalysts were designed for this purpose. Namely, Ran et al.<sup>5</sup> developed frustrated Lewis-pairs via doping boron (Lewis acid) to adsorb and activate  $\text{N}_2$  molecules. Zhang and co-workers<sup>6</sup> were the first to have claimed that the surface oxygen vacancies (OVs) of BiOBr nanosheets may significantly enhance  $\text{N}_2$  the adsorption and activation of  $\text{N}_2$ . Xiong's group<sup>7</sup> introduced heterogeneous Fe atoms into  $\text{TiO}_2$  fibers to stabilize OVs and tune local electronic structure of catalysis for boosting pNRR performance. Furthermore, Yu and coworkers<sup>8</sup> reported that hot electrons generated from plasmon excitation of the Au nanocrystals can facilitate the fracture of the  $\text{N} \equiv \text{N}$  bond to boost  $\text{NH}_3$  synthesis. Although some progress has been achieved on  $\text{N}_2$  photofixation, active photocatalysts with efficient  $\text{N}_2$  adsorption and activation sites are still urgently to expand.

As the foundation of  $\text{N}_2$  molecule activation involves the electron back-donation into the antibonding orbitals of the adsorbate, its prerequisite to achieving efficacious pNRR is to create excellent adsorption

sites<sup>9,10</sup>. Hence, the activity of pNRR is largely reliant upon that adsorption mode of N<sub>2</sub> molecules on the surface active sites of photocatalyst<sup>11</sup>. For instance, N<sub>2</sub> molecules are usually adsorbed on the single-metal sites of semiconductors via a terminal end-on mode<sup>1,9</sup>. The electronic pairing of the d orbitals of the metal sites and the p orbitals of the N<sub>2</sub> molecules allows N<sub>2</sub> molecules to accept electrons from metal sites, causing the adsorbed N<sub>2</sub> to become polarized<sup>12,13</sup>. On the basis of the terminal end-on mode, the effect of the single-metal sites upon molecular polarization may not be sufficient for inert N<sub>2</sub> molecules to be activated. Apparently, the side-on adsorption with a “\*N ≡ N\*” configuration (\*presents the adsorption site) will be more advantageous to weakening the N ≡ N bond for improving pNRR pathway, whereas the end-on configuration formed by the coordination of an individual N atom on a single active site (“\*N ≡ N”) is not<sup>12</sup>. In this regard, might open up fresh avenues for developing high-efficiency pNRR catalysts.

Herein, we first report a large proportion of semi-encapsulated palladium nanoparticles decorated mesoporous TiO<sub>2</sub> nanorods (denoted as se-Pd/m-TiO<sub>2</sub> NRs) toward N<sub>2</sub> photofixation under ambient conditions. The se-Pd NPs (~ 12.2 nm) were modified into m-TiO<sub>2</sub> NRs by an in-situ sodium borohydride (NaBH<sub>4</sub>) reduction method (depicted in Fig. 1a). Simultaneously, the semi-encapsulated Au (~ 10.1 nm) and Pt NPs (~ 9.6 nm) loaded onto m-TiO<sub>2</sub> NRs (denoted as se-Au/m-TiO<sub>2</sub> NRs and se-Pt/m-TiO<sub>2</sub> NRs, respectively) were prepared under certain heating conditions by the same method. Moreover, the full-encapsulated Pd (~ 4.7 nm), Au (~ 6.2 nm) and Pt NPs (~ 3.5 nm) with a small size decorated m-TiO<sub>2</sub> NRs (fe-Pd/m-TiO<sub>2</sub> NRs) were specially prepared for better comparison of pNRR. On the one hand, the se-Pd, Au, and Pt NPs with a larger size are anchored in the irregular pores of m-TiO<sub>2</sub> NRs to form a stable semi-embedding structure; which results in sufficient plasma interaction interface of these noble-metal NPs and m-TiO<sub>2</sub> NRs supports, as well as abundant active sites of N<sub>2</sub> are exposed. The semi-encapsulated structure is better than that of full-encapsulated for the acceleration of N<sub>2</sub> mass transfer, effective absorption of light and efficient separation of interfacial high-energy carriers. On the other hand, the optimal se-Pd/m-TiO<sub>2</sub> NRs possesses abundant bimetallic Ti-Pd active centers at the TiO<sub>2</sub> (101)/Pd (111) interface, which can coordinate with N<sub>2</sub> to form a side-on bridging mode, whereas the N<sub>2</sub> molecules can only adsorb at the single metal Ti sites or Pt sites at the interface of se-Au/m-TiO<sub>2</sub> NRs and se-Pt/m-TiO<sub>2</sub> NRs to form an end-on mode. Further theoretical simulations unravel that the asymmetrical electron donation from Ti and Pd to both-end N atoms of N<sub>2</sub> considerably polarizes the bond of N ≡ N and reduce the activation energy barrier of pNRR pathway. Consequently, the well-designed se-Pd/m-TiO<sub>2</sub> NRs photocatalyst is able to obtain a high rate of NH<sub>3</sub> production (635.73 μg g<sub>cat.</sub><sup>-1</sup> h<sup>-1</sup>) than that of m-TiO<sub>2</sub> NRs (25.52 μg g<sub>cat.</sub><sup>-1</sup> h<sup>-1</sup>), the semi-encapsulated structure including se-Au/m-TiO<sub>2</sub> NRs (75.51 μg g<sub>cat.</sub><sup>-1</sup> h<sup>-1</sup>) and se-Pt/m-TiO<sub>2</sub> NRs (367.84 μg g<sub>cat.</sub><sup>-1</sup> h<sup>-1</sup>), the full-encapsulated construction of fe-Pd/m-TiO<sub>2</sub> NRs (406.42 μg g<sub>cat.</sub><sup>-1</sup> h<sup>-1</sup>), fe-Au/m-TiO<sub>2</sub> NRs (37.31 μg g<sub>cat.</sub><sup>-1</sup> h<sup>-1</sup>) and fe-Pt/m-TiO<sub>2</sub> NRs (255.22 μg g<sub>cat.</sub><sup>-1</sup> h<sup>-1</sup>) in pure water.

## Results

**Chemical structure characterization.** The structures and morphologies of the as-prepared photocatalysts were observed with the aid of SEM and TEM at various magnifications. As displayed in Supplementary Fig. 1a, the SEM imaging of TiO<sub>2</sub> NFs demonstrating the typical electrospun nano-fiber morphology with uniform and smooth. The flexible TiO<sub>2</sub> NFs before annealing were continuous with an average diameter about 200 nm centered in the range of 70–310 nm (Supplementary Fig. 1b). After that, the rough surface of m-TiO<sub>2</sub> NRs with average diameter about 108 nm were obtained by calcination of the TiO<sub>2</sub> NFs in air to remove organic components and then further grinding, as can be seen from Supplementary Fig. 1c. As depicted in high-resolution TEM image of Fig. 1b, the irregular pores of the m-TiO<sub>2</sub> NRs (Marked with cyan dotted line) as well as a good crystallinity of the m-TiO<sub>2</sub> NRs with a 0.352 nm lattice spacing which matches (101) diffraction facet of anatase TiO<sub>2</sub> could be clearly observed. Simultaneously, the TEM, HRTEM and EDS element mapping were further used for analyzing the structure, composition, and distribution of cocatalysts (e.g., se-Pd NPs etc.) on the TiO<sub>2</sub> NRs. It can be evidently seen from the TEM image that a large proportion of se-Pd NPs (~ 12.2 nm) are uniformly distributed on the m-TiO<sub>2</sub> NRs support in a semi-encapsulated structure (Fig. 1c and Fig. 2a). Notably, the HRTEM images more accurately and intuitively testified the successful preparation of the semi-encapsulated art configuration between Pd NPs and TiO<sub>2</sub> support (Fig. 1d). As indicated by the inset of Fig. 1d, these se-Pd NPs had a lattice spacing of 0.224 nm, corresponding to the (111) facet of metallic Pd as well as confirming that these NPs were well-defined Pd particles<sup>14,15</sup>. Analogously, the XRD assessments were conducted for demonstrating the phase structure of the as-prepared samples. As displayed in supplementary Fig. 1d, the diffraction patterns of the m-TiO<sub>2</sub> NRs samples match well with that of anatase phase TiO<sub>2</sub> (PDF#21-1272, Anatase, syn). After se-Pd NPs loaded on the m-TiO<sub>2</sub> NRs, the peaks of metallic Pd phase could be found from XRD patterns of the corresponding samples. The very weak peak at around 40.12° could be attributed to the Pd (111) reflection, in good agreement with HRTEM results (Inset of Supplementary Fig. 1d). To verify the presence and distribution of Pd NPs in the as-prepared catalyst, elemental energy-dispersive X-ray spectroscopy (EDS) mapping (Fig. 1e-h) was implemented for analyzing the sample, revealing that Pd mainly distributes the surface of the entire architecture. In addition, the as-prepared m-TiO<sub>2</sub> NRs modified with se-Au NPs (~ 10.1 nm), se-Pt NPs (~ 9.6 nm), fe-Pd NPs (~ 4.7 nm), fe-Au NPs (~ 6.2 nm) and fe-Pt NPs (~ 3.5 nm) are clearly identified and visualized by TEM and TEM-EDS mapping (Fig. 2c-f and Supplementary Fig. 2–4).

The high-resolution spectra of XPS regarding Ti 2p, O 1s and Pd 3d were interrogated particularly for determining the chemical state and surface composition of m-TiO<sub>2</sub> NRs and se-Pd/m-TiO<sub>2</sub> NRs catalysts. About high-resolution XPS spectrum concerning Ti 2p of m-TiO<sub>2</sub> NRs (Fig. 3a), two peaks were observed at 458.32 eV (Ti 2p<sub>3/2</sub>) and 464.02 eV (Ti 2p<sub>1/2</sub>), and could be earmarked to Ti<sup>4+</sup> states<sup>16</sup>. As for the high-resolution XPS spectrum of O 1s (Fig. 3b), the peaks located at 529.56, 531.42, and 532.7 eV are earmarked to oxygen related to O species in the lattice (O<sub>L</sub>), O species vicinal the defects or vacancies (O<sub>V</sub>), and dissociated or chemisorbed (O<sub>C</sub>) species<sup>17,18</sup>. Nevertheless, for the se-Pd/m-TiO<sub>2</sub> NRs sample, the binding energy of Ti 2p and O 1s was shifted to a greater value, suggesting a potent interaction

between se-Pd NPs and m-TiO<sub>2</sub> NRs<sup>19,20</sup>. Figure 3c depicts the Pd 3d spectrum of se-Pd/m-TiO<sub>2</sub> NRs. The peaks centered at 336.64 and 341.91 eV demonstrated Pd species with oxide states. The energy of banding at 334.79 and 340.05 eV, relevant to the Pd 3d<sub>5/2</sub> and Pd 3d<sub>3/2</sub> peaks, were earmarked to metallic Pd<sup>21,22</sup>. Hence, the initial Pd species over the catalysts were in the shape of the Pd<sup>0</sup> state. Additionally, the Low-temperature electron paramagnetic resonance (EPR) analysis was implemented for the evaluation of the presence of OVs. As shown in Fig. 3d, a characteristic oxygen vacancies (OVs) signal with a g factor of 2.003 was observed on the individual m-TiO<sub>2</sub> NRs, indicating that OVs could be generated on the surface of m-TiO<sub>2</sub> NRs by high-temperature calcination<sup>23,24</sup>. Meanwhile, compared with m-TiO<sub>2</sub> NRs, the se-Pd/m-TiO<sub>2</sub> NRs show a sharper and stronger OVs signal after semi-encapsulated Pd NPs assembling, which could be attributed to the existence of massive asymmetric OVs at the TiO<sub>2</sub>/Pd interface<sup>25,26</sup>.

To verify the coordination state and electronic structure of Pd in se-Pd/m-TiO<sub>2</sub> NRs, the X-ray absorption near-edge structure (XANES) and X-ray absorption fine structure spectra (EXAFS) were conducted at the Pd K-edge. The spectra of XANES display that the absorption edge of Pd K-edge for se-Pd/m-TiO<sub>2</sub> NRs placed between that of PdO and Pd foil (Fig. 3e), divulging the valence state of Pd is between 0 and + 2, which may be attribute to the formation of Pd-O or Pd-Ti coordination bond at the TiO<sub>2</sub> (101)/Pd (111) interface by Pd atoms on the surface of se-Pd NPs.

Meanwhile, the Fourier-transformed *k*<sup>3</sup>-weighted EXAFS spectra (Fig. 3f) confirm the co-existence of Pd-O and Pd-Pd coordination in the se-Pd/m-TiO<sub>2</sub> NRs sample with respect to PdO sample and Pd foil. In the current research, the Pd foil was applied for the validation of the se-Pd NPs in the se-Pd/m-TiO<sub>2</sub> NRs sample. The nature of metallic NPs or Pd bulk is Pd-Pd coordination. Apparent Pd-Pd coordination in se-Pd/m-TiO<sub>2</sub> NRs was detected, demonstrating the presence of Pd NPs; which is consistent with the TEM and HRTEM data. Moreover, the reference of PdO was employed for testifying the contributor of Pd-O coordination. In regard to se-Pd/m-TiO<sub>2</sub> NRs, only Pd-O coordination can be observed and no Pd-O-Pd coordination existed. Thus, the Pd-O coordination mode in the sample is different from that of PdO phase. Besides, the bond lengths at 3.14 Å corresponding to Pd-Ti are identified in se-Pd/m-TiO<sub>2</sub> NRs (Supplementary Table 2), suggesting the existence of Pd-Ti coordination bond in proximity to Ti atoms at the TiO<sub>2</sub> (101)/Pd (111) interface. The plot of wavelet transform of se-Pd/m-TiO<sub>2</sub> NRs shows that one notable peak was observed at ~ 6 Å<sup>-1</sup> (Fig. 3g), which corresponds to the Pd-O bonding through the comparison of PdO and Pd foil counterparts. Meanwhile, the faintish peaks of Pd-Ti and Pd-Pd with intensity maxima at ca. 7 Å<sup>-1</sup> and above 9 Å<sup>-1</sup> were also observed (Fig. 3g), which matches well with the EXAFS results. On the basis of previous reports and Supplementary Table 2, the plentiful Pd-O coordination (2.07 Å) is earmarked to Pd-O-Ti species<sup>27</sup>, contributed through the interfacial between TiO<sub>2</sub> (101) and se-Pd NPs<sup>28</sup>. More importantly, a large number of Pd-O and Pd-Ti bonds were formed at the TiO<sub>2</sub> (101)/Pd (111) interface, resulting in the anchoring structure of se-Pd NPs and m-TiO<sub>2</sub> NRs has a good stability.

The optical characteristics of the ingeniously constructed catalysts were examined through UV-vis DRS spectra (Fig. 4a). The m-TiO<sub>2</sub> NRs exhibit a steep absorption edge placed at ~ 380 nm and are in agreement with the intrinsic bandgap absorption of anatase TiO<sub>2</sub> (~ 3.2 eV)<sup>29</sup>. Loading on m-TiO<sub>2</sub> NRs with semi- or full-encapsulated NPs (e.g., Pd, Au, and Pt NPs) will result in a shift to the visible range, which could be attributed to the generation of metallic gray or lattice plasmons in these samples<sup>30,31</sup>. Notably, decorating m-TiO<sub>2</sub> NRs with se-Pd NPs demonstrate a stronger and wider band of absorption in the visiblelight region (from 400 to 800 nm) than other configurations of noble metal decorated-TiO<sub>2</sub> NRs.

To deeper understanding the local electric field enhancement of these catalysts by the the localized surface plasmon resonance (LSPR) effect, the finite-difference time-domain (FDTD) simulations were carried out to assess the spatial distribution of local electric-field intensity at the interface between plasmonic metal NPs and m-TiO<sub>2</sub> NRs as a function of incident light wavelength. The electric field at the interface of se-Pd, Au, Pt/m-TiO<sub>2</sub> NRs were stronger than that of fe-Pd, Au, Pt/m-TiO<sub>2</sub> NRs. The interface between the se-Pd NPs and m-TiO<sub>2</sub> NRs was “hot” at an excitation wavelength of 650 nm (Fig. 4d-i); this high field intensity suggested more charge-carrier formation<sup>32,33</sup>. More interestingly, at an excitation wavelength of 550 nm, the electric field intensity at the interface of the se-Pd/m-TiO<sub>2</sub> NRs is still comparable to that of se-Au/m-TiO<sub>2</sub> NRs as well as far superior to that of fe-Au/m-TiO<sub>2</sub> NRs, although the Au NPs possess an excellent SPR characteristic peak at about 550 nm (Fig. 2g-h, and Supplementary Fig. 4h). Therefore, the interface of se-Pd/m-TiO<sub>2</sub> would be high-efficient catalytic hotspots of pNRR.

With the intention of exploring in-depth the kinetic behaviors of carriers, the steady-state photoluminescence (PL) measurements were carried out. The PL signals of the catalyts are determined under an excitation light of 365 nm as shown in Fig. 4b. In comparison to the potent emission peak of m-TiO<sub>2</sub> NRs, the metallic granular-TiO<sub>2</sub> composites demonstrate a rather weaker PL peak, illustrating that the modification plasmonic metal NPs could effectively limit electron-hole recombination<sup>34,35</sup>. Of theses, the se-Pd/m-TiO<sub>2</sub> NRs sample possesses the lowest peak intensity, manifesting the highest separation rate of the photogenerated charge carriers. Relative to the time-resolved photoluminescence decay measurements for the other samples (Supplementary Fig. 5 and Table 3), the se-Pd/m-TiO<sub>2</sub> NRs display the longest average decay times of 10.44 ns, indicating that this unique exquisite mode is beneficial for promoting the lifetime of photogenerated electrons.

The Brunauer-Emmett-Teller (BET) surface area and pore structure of the synthesized catalysts were studied by nitrogen adsorption-desorption. As shown in Supplementary Fig. 6, all the samples take possession of a stepwise adsorption/desorption hysteresis, illustrated throughr type IV isotherms, which has the features of mesoporous materials<sup>36</sup>. The variations in BET surface area and average pore size following the plasmonic metal NPs modification was summarized in Supplementary Table 4. The reduction of BET specific surface area was due to the slight blockage of pores in m-TiO<sub>2</sub> NRs after modification of these NPs<sup>37</sup>. Besides, the average pore size of the prepared catalysts was determined by Barrett–Joyner–Halenda (BJH) approach (Insets of Supplementary Fig. 6, Supplementary Table 4). In

general, it can be found that the average pore size of TiO<sub>2</sub> NRs modified with larger NPs tends to be enlarged, while smaller NPs tends to be reduced. Such phenomenon could be attributed to the extrusion of the larger NPs on the irregular pores of the substrate TiO<sub>2</sub> during the nucleation and growth<sup>38,39</sup>.

To further understand the pNRR activity of se-Pd/m-TiO<sub>2</sub> NRs, the essence of catalytic active site was revealed by temperature-programmed desorption of N<sub>2</sub> (N<sub>2</sub>-TPD) on catalyst surfaces (Fig. 4c). The peak of desorption at about 150 °C for N<sub>2</sub> physisorption was detected for these catalysts and the integral intensity of peak (i.e., peak area, mean the amount of the physically adsorbed N<sub>2</sub>) was positively correlated with the catalyst specific surface area (Supplementary Fig. 6 and Table 4). Both se-Pd/m-TiO<sub>2</sub> NRs and fe-Pd/m-TiO<sub>2</sub> NRs represented a desorption peak at about 420 °C for N<sub>2</sub> chemisorption, while the se- and fe-Pt/m-TiO<sub>2</sub> NRs possess a lower chemisorption desorption peak at about 450 °C. Besides, the negligible N<sub>2</sub> chemisorption of m-TiO<sub>2</sub> NRs, se-Au/m-TiO<sub>2</sub> NRs and fe-Au/m-TiO<sub>2</sub> NRs accounts for their poor adsorption sites. N<sub>2</sub> chemisorption is the prerequisite for photocatalytic activation of N<sub>2</sub>. Accordingly, the se-Pd/m-TiO<sub>2</sub> NRs catalyst with more chemically adsorbed N<sub>2</sub> is responsible for the higher NH<sub>3</sub> production. Thus, the well-designed se-Pd/m-TiO<sub>2</sub> NRs presents a good visible light response, greatly promoted energetic charge carriers separation efficiency, effective and abundant N<sub>2</sub> adsorption sites, which are beneficial for pNRR.

**Photocatalytic performance.** The photocatalytic N<sub>2</sub> fixation performance of the as-prepared samples appraised by employing water as the solvent and proton source under full spectrum through spectrophotometrically measurement of the generated NH<sub>3</sub> with indophenol indicator (Supplementary Fig. 7). To eliminate the interference of environmental adsorption of NH<sub>3</sub>, the photocatalyst suspension was in succession bubbled with N<sub>2</sub> prior to the light radiation for at least 30 min. The se-Pd/m-TiO<sub>2</sub> NRs sample shows an excellent NH<sub>3</sub> production rate of 635.73 μg g<sub>cat.</sub><sup>-1</sup> h<sup>-1</sup> under full spectrum light irradiation (Fig. 5a), which is about 24.91, 8.42, 1.73, 1.56, 17.04, and 2.49 times higher than that of m-TiO<sub>2</sub> NRs (25.52 μg g<sub>cat.</sub><sup>-1</sup> h<sup>-1</sup>), se-Au/m-TiO<sub>2</sub> NRs (75.51 μg g<sub>cat.</sub><sup>-1</sup> h<sup>-1</sup>), se-Pt/m-TiO<sub>2</sub> NRs (367.84 μg g<sub>cat.</sub><sup>-1</sup> h<sup>-1</sup>), fe-Pd/m-TiO<sub>2</sub> NRs (406.42 μg g<sub>cat.</sub><sup>-1</sup> h<sup>-1</sup>), fe-Au/m-TiO<sub>2</sub> NRs (37.31 μg g<sub>cat.</sub><sup>-1</sup> h<sup>-1</sup>), and fe-Pt/m-TiO<sub>2</sub> NRs (255.22 μg g<sub>cat.</sub><sup>-1</sup> h<sup>-1</sup>), respectively. Moreover, several rigorous contrast experiments were performed for the elimination of the probable contamination from the ambient environment (Fig. 5b). When the photocatalytic procedure was conducted under Ar ambient or in the dark condition, just trace NH<sub>3</sub> could be observed, suggesting that the generated NH<sub>3</sub> over se-Pd/m-TiO<sub>2</sub> NRs indeed originates from the photocatalytic reaction. Besides, no N<sub>2</sub>H<sub>4</sub> was detected during the process (Supplementary Fig. 8c), demonstrating an excellent selectivity for NH<sub>3</sub> production.

In addition, the stability of se-Pd/m-TiO<sub>2</sub> NRs was investigated through recycling the catalyst (Fig. 5c). Following eight consecutive reaction rounds, approximately 92.37% of its original catalytic activity was retained, indicating remarkable catalytic stability. To appraise the efficiency of light utilization, the apparent quantum efficiency (AQE) of se-Pd/m-TiO<sub>2</sub> NRs was estimated under the irradiation of

monochromatic light (Supplementary Fig. 10a). In particular, the AQE was implemented to be 0.37% at 375 nm for se-Pd/m-TiO<sub>2</sub> NRs, much higher than many reported results (Supplementary Table 5). Hence, the se-Pd/m-TiO<sub>2</sub> NRs catalyst presents one of the best performances of photocatalytic N<sub>2</sub> fixation reported to date (Supplementary Table 6).

For demonstrating whether photocatalytic N<sub>2</sub> fixation on the se-Pd/m-TiO<sub>2</sub> NRs was authentic, the photocatalytic N<sub>2</sub> fixation under <sup>15</sup>N isotope-labeled N<sub>2</sub> (with the purity not lower than 99%) was conducted. The generated NH<sub>4</sub><sup>+</sup> is capable of reacting with phenol and hypochlorite for the formation of <sup>15</sup>N-labeled indophenol<sup>40,41</sup>, which could be evaluated accurately via a liquid chromatography-mass spectrometry (LC-MS). Supplementary Fig. 11a depicts a vigorous mass spectroscopy signal of <sup>14</sup>N-labeled indophenol anion at 198 m/z in LC-MS investigation when employing <sup>14</sup>N<sub>2</sub> as the feeding gas. Of note, the <sup>15</sup>N-labeled indophenol negative anion displays a remarkable enhanced mass spectrum signal at approximately 199 m/z in LC-MS analysis (Supplementary Fig. 11b). The signal gives a greater intensity relevant to the <sup>14</sup>N:<sup>15</sup>N natural abundance ratio following 30 min illumination. These data identify that the generate ammonium ion explored in the current research emanated from N<sub>2</sub> photofixation.

To meticulously verify that the pNRR occurred on the surface of se-Pd/m-TiO<sub>2</sub> NRs, time-dependent *in-situ* Fourier-transform infrared (FTIR) assessments were executed to investigate the surface intermediates formed during the pNRR process (See Supplementary Fig. 10b). Within the photoreaction for instance under the irradiation of light over se-Pd/m-TiO<sub>2</sub> NRs, diverse signals amplified with the time of reaction (Fig. 5d). Peaks at about 3555 cm<sup>-1</sup> (i) and 3240 (ii) cm<sup>-1</sup> could promptly be earmarked to asymmetric ν(N-H) stretching modes of NH<sub>3</sub>, while the two absorption bands at 1713 cm<sup>-1</sup> (v) and 1667 cm<sup>-1</sup> (vii) were allocated to the bending mode of σ(N-H)<sup>42,43</sup>. Analogously, peaks at ~ 1750 cm<sup>-1</sup> (iv) and ~ 1470 cm<sup>-1</sup> (viii) are σ(H-N-H) bending vibration of NH<sub>3</sub><sup>44</sup>. The signal at about 2873 cm<sup>-1</sup> (iii) and 1654 cm<sup>-1</sup> (vi) correspond to an antisymmetric deformation vibration of NH<sub>4</sub><sup>+</sup>. The intensity of these signals firstly increased and then stabilized over time, indicating that NH<sub>3</sub> or NH<sub>4</sub><sup>+</sup> were continuously formed on the surface of se-Pd/m-TiO<sub>2</sub> NRs, which provides an adequate evidence for pNRR procedure.

**The pNRR mechanisms.** To gain atomic-level insights into N<sub>2</sub> photofixation, the probable coordination geometry of N<sub>2</sub> on the surfaces of TiO<sub>2</sub> (101), Pd (111), OVs-TiO<sub>2</sub> (101)/Pd (111), TiO<sub>2</sub> (101)/Pd (111) interface (Supplementary Fig. 12); Au (111), OVs-TiO<sub>2</sub> (101)/Au (111) and TiO<sub>2</sub> (101)/Au (111) interface (Supplementary Fig. 13); Pt (111), OVs-TiO<sub>2</sub> (101)/Pt (111) and TiO<sub>2</sub> (101)/Pt (111) interface (Supplementary Fig. 17) was investigated by the density functional theory (DFT) calculations. The configuration of optimized adsorption for a molecule of N<sub>2</sub> is a distal end-on mode on TiO<sub>2</sub> (101), Pd (111), Au (111), Pt (111), OVs-TiO<sub>2</sub> (101)/Pd (111), OVs-TiO<sub>2</sub> (101)/Au (111), single Ti sites at the TiO<sub>2</sub> (101)/Au (111) interface, OVs-TiO<sub>2</sub> (101)/Pt (111), single Pt sites at the TiO<sub>2</sub> (101)/Pt (111) interface and a side-on bridging mode on Ti-N<sub>2</sub>-Pd dual sites at the TiO<sub>2</sub> (101)/Pd (111) interface (Fig. 6,

Supplementary Fig. 14 and Supplementary Fig. 18). The energy of adsorption for the N<sub>2</sub> side-on bridged on bimetallic Ti-Pd centers (-0.64 eV) is excel than that for the N<sub>2</sub> end-on bound to a Ti sites of TiO<sub>2</sub> (-0.29 eV), Pd site of Pd (111) (-0.48 eV), OVs-TiO<sub>2</sub> (101)/Pd (111) (-0.56 eV), OVs-TiO<sub>2</sub> (101)/Au (111) (-0.42 eV), Ti sites at TiO<sub>2</sub> (101)/Au (111) interface (-0.38 eV), OVs-TiO<sub>2</sub> (101)/Pt (111) (-0.43 eV), and Pt sites at TiO<sub>2</sub> (101)/Pt (111) interface (-0.51 eV) (Fig. 8a and Supplementary Fig. 21). However, the OVs with respect to a single metal site was thermodynamically desirable for the activation of N≡N bond, demonstrating the rationality of general defect engineering strategy<sup>45</sup>, the bimetallic Ti-Pd center illustrated substantial dominance to the OVs.

To further insight into the differences of two N atoms (N1 and N2) at the various models, the differential charge diagram was employed for reflecting the polarization of adsorbed N<sub>2</sub> molecule. The charge discrepancy between two adsorbed N atoms on Ti-Pd dual sites was 0.11e (-0.15|e| vs -0.26|e|), which is greater than 0.02e (0|e| vs -0.02|e|) for N<sub>2</sub> adsorbed on Ti sites of TiO<sub>2</sub> (101), 0.07e (-0.02|e| vs -0.09|e|) for N<sub>2</sub> adsorbed on Pd sites of Pd (111), 0.10e (-0.21|e| vs -0.11|e|) for N<sub>2</sub> adsorbed on OVs of TiO<sub>2</sub> (101)/Pd (111), 0.05e (-0.06|e| vs -0.01|e|) for N<sub>2</sub> adsorbed Ti sites at TiO<sub>2</sub> (101)/Au (111) interface, as well as 0.08e (-0.14|e| vs -0.06|e|) Pt sites at TiO<sub>2</sub> (101)/Pt (111) interface (Fig. 7, Supplementary Fig. 15 and Supplementary Fig. 19), indicative of more efficacious polarization of the N<sub>2</sub> adsorbed on Ti-Pd dual sites.

Meanwhile, Fig. 8b illustrates that the electrons could be preferably agglomerated on the atom of N1 bonded with Ti-end at the bimetallic Ti-Pd active centers. This type of imbalanced charge distribution differentiates the two atoms of N for adsorbed N<sub>2</sub>, initiating the associative distal pathway at the Ti-end of Ti-Pd dual sites<sup>7</sup>. For deeper comprehending the polarization effect of Ti-Pd dual sites on adsorbed N<sub>2</sub> molecules, the bond length of N≡N bond was also used as the descriptor for polarization of N<sub>2</sub> molecules. As displayed in Fig. 8c, the bond of N≡N for N<sub>2</sub> bridged on Ti-Pd dual sites was enhanced to 1.222 Å, analogous to the double bond lengths of azobenzene (PhN = NPh) (1.255 Å) and diazene (HN = NH) (1.201 Å)<sup>11</sup>. On the contrary, the N-N bond lengths of N-N for N<sub>2</sub> adsorbed on single metal sites (e.g., Ti, Pd, Au and Pt) or OVs is equivalent to that of free N<sub>2</sub> (1.155 Å), holding a triple-bond order (Fig. 8c and Supplementary Fig. 22). Therefore, the effective N<sub>2</sub> adsorption with bimetallic Ti-Pd center of se-Pd/m-TiO<sub>2</sub> NRs is beneficial for boosting the activity in pNRR.

The N bridged on Ti-end of Ti-Pd center illustrated a greater electron density and subsequently it was more simply hydrogenated in comparison to that on Pd-end (Fig. 8b). Futhermore, protonation initiating from N on Ti is an obvious process of gradually lengthening the N≡N bond, resulting in the formation of NH<sub>3</sub>, whereas protonation starting from Pd does not (Fig. 8d). Then, the Gibbs free-energy diagrams of pNRR pathways relative to se-Pd/m-TiO<sub>2</sub> NRs with Ti-Pd dual sites were unfolded (Fig. 8e). The initial adsorption of N<sub>2</sub> bridged on Ti-Pd dual sites releases 0.11 eV of free energy and polarizes N<sub>2</sub> molecule with charge redistribution. The Gibbs free energy change ( $\Delta G$ ) for the hydrogenation of \*N-N to \*HN-N (blue line) was only 0.57 eV (from -0.11 to 0.46 eV), while \*N-N was hydrogenated to \*N-NH with the  $\Delta G$

of 0.75 eV (from -0.11 to 0.64 eV). Next, the subsequent hydrogenation process including \*N-HN to \*NH-NH ( $\Delta G = -0.39$  eV), \*NH-NH to \*NH<sub>2</sub>-NH ( $\Delta G = -0.13$  eV) and \*NH<sub>2</sub>-NH to \*NH<sub>3</sub>-NH ( $\Delta G = -0.84$  eV) steps relative to the optimized pNRR procedure (blue line) is facile because the  $\Delta G$  values of these process are negative. Inversely, the other possibilities of pNRR paths (gray line) containing \*N-HN to \*NH<sub>2</sub>-N, \*NH-NH to \*NH-NH<sub>2</sub>, and \*NH<sub>2</sub>-NH to \*NH<sub>2</sub>-NH<sub>2</sub> (gray line,  $\Delta G$  values are 0.27, 0.31 and -0.22 eV, respectively) require overcoming a certain reaction energy barrier or hold a lower  $\Delta G$  compare to the optimal pNRR process. Afterwards, the first NH<sub>3</sub> molecule formed at the Ti-end of Ti-Pd dual sites absorbs the energy of 0.1 eV and further releases. Eventually the remaining N atom adsorbed on the Pd-end of Ti-Pd dual sites undergoes a continuous hydrogenation process such as \*NH to \*NH<sub>2</sub> ( $\Delta G = -1.06$  eV) and \*NH<sub>2</sub> to \*NH<sub>3</sub> ( $\Delta G = -0.06$  eV) paths then overcome a reaction energy barrier of 0.88 eV to release the second NH<sub>3</sub> molecule. Taken together, the unbalanced charge difference of N<sub>2</sub> molecule adsorbed at the Ti-Pd dual sites enables the pNRR process develop a distal association path dominated by the Ti-end, which greatly diminishes the barrier of activation energy and improves photocatalytic NH<sub>3</sub> synthesis efficiency.

## Discussion

In summary, we first develop a large proportion of semi-encapsulated Pd NPs decorated m-TiO<sub>2</sub> NRs towards high-performance photocatalytic N<sub>2</sub> to NH<sub>3</sub> under ambient conditions. This unique anchoring structure formed by the se-Pd NPs and m-TiO<sub>2</sub> NRs fully exposes the bimetallic Ti-Pd centers at the TiO<sub>2</sub> (101)/Pd (111) interface, and simultaneously possesses an excellent structural stability. The two N atoms in adsorbed N<sub>2</sub> are bridged to the center of Ti-Pd, and the asymmetrical electron donation from the atoms of Ti and Pd to N<sub>2</sub> adsorbate could effectively stretch the N  $\equiv$  N bond even to the level of double bond. Owing to the synergistic effect of Ti-Pd dual sites, the potential activation energy barrier of N<sub>2</sub> is decreased, as verified through DFT calculations. As a result, the optimized and screened se-Pd/m-TiO<sub>2</sub> NRs (2.71%) photocatalyst demonstrates a remarkable ammonia (NH<sub>3</sub>) production rate of 635.73  $\mu\text{g g}_{\text{cat}}^{-1} \text{h}^{-1}$ , attaining a considerable apparent quantum efficiency (AQE) of 0.37% at 375 nm in the absence of any sacrificial agent. This work not only paves the way to expand high-performance catalysts for N<sub>2</sub> photofixation under mild circumstances through regulating bimetallic centers, but also offers an atomic-level perspective for comprehending the internal pNRR procedure.

## Methods

**Chemicals.** Tetrabutyl titanate (TBT), Polyvinylpyrrolidone (PVP, M.W. = 1,300,000), Labeled <sup>15</sup>N<sub>2</sub> gas, Phenol nitroprusside solution, alkaline hypochlorite solution, hydrazine hydrate (N<sub>2</sub>H<sub>4</sub>·H<sub>2</sub>O, 50%), para-(dimethylamino) benzaldehyde (p-C<sub>9</sub>H<sub>11</sub>NO), dimethyl sulfoxide-d<sub>6</sub> (DMSO-D<sub>6</sub>) and N, N-dimethylformamide (DMF) were obtained from Sigma-Aldrich Chemical Company. Palladium(II) chloride (PdCl<sub>2</sub>), Chloroauric acid (HAuCl<sub>4</sub>·4H<sub>2</sub>O), hexachloroplatinic acid (H<sub>2</sub>PtCl<sub>6</sub>·6H<sub>2</sub>O), Sodium borohydride (NaBH<sub>4</sub>), Ammonium chloride (NH<sub>4</sub>Cl), Sodium hydroxide (NaOH) and Acetic acid (HAc, > 97%) were

bought from Shanghai Macklin Biochemical Co. Ltd. The reagents were analytically pure (AR) and implemented as received without additional purifications. Deionized water was used in all the assessments.

**Preparation of mesoporous TiO<sub>2</sub> nanorods.** The mesoporous TiO<sub>2</sub> nanorods (m-TiO<sub>2</sub> NRs) were obtained via a spinneret electrospinning process with subsequent calcination and trituration. First, the TiO<sub>2</sub> nanofibers (TiO<sub>2</sub> NFs) were synthesized according to previous reports with minor improvements<sup>46–48</sup>. Briefly, polyvinylpyrrolidone (PVP) was added to ethanol, and stirred for 12 h at ambient temperature to form a transparent solution (14 wt%). Next, tetrabutyl titanate (TBT), ethanol and acetic acid were mixed at a mol. ratio of 1 : 3 : 3, and stirred in an ice-water bath for 30 min. The above two solutions were mixed at a wt. ratio of 1 : 1, and stirred over night to obtain a precursor solution. The precursor solution was electrospun by using spinning equipment (QZNT-E01) at an electrostatic voltage of 19 kV and a propulsion rate of 0.7 mL h<sup>-1</sup>. The electrospinning temperature was 25°C, the relative humidity was 45 ± 5%, and the reception distance was 11 cm. Second, the TiO<sub>2</sub> nanofibers was calcined via a two-stage progressive heating procedure: 2°C/min from ambient temperature to 240°C as well as kept 240°C for 4 h under air atmosphere to allow the stabilization to complete, 2°C/min from 240°C to 500°C as well as kept 500°C for 3 h under air atmosphere to allow the carbonization to achieve<sup>49,50</sup>. Finally, the calcined samples were collected and further ground into uniform powder for further use.

**Preparation of semi-encapsulated Pd/m-TiO<sub>2</sub> NRs, Au/m-TiO<sub>2</sub> NRs and Pt/m-TiO<sub>2</sub> NRs.** The semi-encapsulated Pd/m-TiO<sub>2</sub> NRs (se-Pd/m-TiO<sub>2</sub> NRs) were synthesized through a NaBH<sub>4</sub> reduction method. Typically, 100 mg of m-TiO<sub>2</sub> NRs were dispersed in 50 mL deionized water and mixed with certain amount of PdCl<sub>2</sub> with different mass ratios (x%-Pd/m-TiO<sub>2</sub> NRs, x = 0, 1, 3, 5 and 7, respectively). After stirring 30 min, a fresh NaBH<sub>4</sub> solution (0.01 M, 20 mL) were added into the above solution by dropwise with stirring constantly continued at room temperature for 30 min. Next, the resulting solution was collected, rinsed with ethanol and deionized water thoroughly, and then dried at 60°C for later use. The semi-encapsulated Au/mTiO<sub>2</sub> NRs (se-Au/m-TiO<sub>2</sub> NRs) with a mass ratio of 3% was synthesized by the NaBH<sub>4</sub> reduction method except that PdCl<sub>2</sub> was replaced with HAuCl<sub>4</sub>·4H<sub>2</sub>O at 60 °C for stirring 30 min. Similarly, The semi-encapsulated Pt/m-TiO<sub>2</sub> NRs (se-Pt/m-TiO<sub>2</sub> NRs) was prepared via NaBH<sub>4</sub> reduction method except that PdCl<sub>2</sub> was replaced with H<sub>2</sub>PtCl<sub>6</sub>·6H<sub>2</sub>O under 80 °C condition for stirring 30 min. In addition, the composition of the x%-Pd/m-TiO<sub>2</sub> and the semi-encapsulated metal NPs loaded on the m-TiO<sub>2</sub> NRs with a mass ratio of 3% were determined by the ICP-OES (Supplementary Table 1), which is consistent with the desired loading level.

**Synthesis of full-encapsulated Pd/m-TiO<sub>2</sub> NRs, Au/m-TiO<sub>2</sub> NRs and Pt/m-TiO<sub>2</sub> NRs.** The full-encapsulated Pd NPs with small size decorated m-TiO<sub>2</sub> NRs (fe-Pd/m-TiO<sub>2</sub> NRs) were specially prepared for better comparison. In brief, 100 mg of m-TiO<sub>2</sub> NRs were dispersed in 50 mL deionized water and mixed with 3 wt% PdCl<sub>2</sub>. After stirring 30 min, a fresh NaBH<sub>4</sub> solution (0.01 M, 20 mL) were added into the above mixture by dropwise under a bath of ice and stirred constantly for 30 min. Afterwards the mixture

was collected, and washed with ethanol and deionized water thoroughly, and dried at 60°C for further use. Moreover, The preparation of full-encapsulated Au/mTiO<sub>2</sub> NRs (fe-Au/m-TiO<sub>2</sub> NRs) and Pt/m-TiO<sub>2</sub> NRs (fe-Pt/m-TiO<sub>2</sub> NRs) with a mass ratio of 3% were fabricated through the same procedure of “Preparation of semi-encapsulated Pd/m-TiO<sub>2</sub> NRs” except that PdCl<sub>2</sub> was replaced with HAuCl<sub>4</sub>·4H<sub>2</sub>O and H<sub>2</sub>PtCl<sub>6</sub>·6H<sub>2</sub>O, respectively. Besides, the content of the fe-Pd NPs (3%), Au NPs (3%) and Pt NPs (3%) was measured through the ICP-OES (Supplementary Table 1), which was basically consistent with the load content.

**Screening and optimization of photocatalysts.** To achieve an excellent pNRR performance, the content of se-Pd NPs loaded on m-TiO<sub>2</sub> NRs was optimized by using indophenol as indicator to evaluate the generated NH<sub>3</sub>. As shown in Supplementary Fig. 23a, these catalysts display a volcano-type activity in the yield of NH<sub>3</sub> as a function of Pd content. Particularly, the se-Pd/m-TiO<sub>2</sub> NRs (2.71%) shows the highest NH<sub>3</sub> generation rate of up to 635.73 μg g<sub>cat</sub><sup>-1</sup> h<sup>-1</sup>; among these different Pd-loading catalysts. Meanwhile, the Supplementary Fig. 23b also manifest that the se-Pd/m-TiO<sub>2</sub> NRs (2.71%) possesses a prominent pNRR activity than that of m-TiO<sub>2</sub> NRs, se-Au/m-TiO<sub>2</sub> NRs (2.92%), se-Pt/m-TiO<sub>2</sub> NRs (2.84%), fe-Pd/m-TiO<sub>2</sub> NRs (2.62%), fe-Au/m-TiO<sub>2</sub> NRs (2.76%) and fe-Pt/m-TiO<sub>2</sub> NRs (2.86%). Hence, the optimized se-Pd/m-TiO<sub>2</sub> NRs (2.71%) was denoted as se-Pd/m-TiO<sub>2</sub> NRs and conducted for the characterization and experiments.

**Characterization.** X-Ray diffraction (XRD) patterns of the catalysts were performed on a PANalytical diffractometer using the irradiation of Cu. The elemental compositions and morphologies were analyzed through transmission electron microscopy (TEM, JEOL 2100F) and scanning electron microscopy (SEM, JEOL JSM-7001F). The spectra of absorption were performed employing diffuse reflection spectra (DRS, HITACHI UV-3900). The installation of photochemical reactor (CEL-APR100H) was exerted to CEL-GPPCL system (Beijing China Education Au-light Co., Ltd.) equipped with a 300-W Xe lamp. Furthermore, in N<sub>2</sub> temperature programmed desorption assessments, the chemisorbed N<sub>2</sub> were performed (Micromeritics Auto Chem II) by implementing a TCD as detector. The surface electronic states were scrutinized through X-ray photoelectron spectroscopy (XPS, Thermo ESCALAB 250Xi) with all binding energies referencing to the C 1s peak at 284.8 eV. The curves of transient and steady photoluminescence (PL) for the as-fabricated samples were achieved under the excitation of a hydrogen flash lamp with the wavelength at 800 nm on a FLS1000 fluorescence lifetime spectrophotometer (Edinburgh Instruments, UK). The contents of loaded Pd, Au, and Pt on TiO<sub>2</sub> were ascertained through inductively coupled plasma optical emission spectrometer (ICP-OES, PerkinElmer). The N<sub>2</sub> absorption-desorption properties of the diverse catalysts were determined by Micromeritics ASAP2460 instrument, and the pore size distribution and specific surface area were appraised through BET and BJH approach.

## Declarations

**Competing interests:**

The authors declare no competing interests.

## References

1. Zhao, Z. F. et al. Boosting nitrogen activation via bimetallic organic frameworks for photocatalytic ammonia synthesis. *ACS Catal.* **11**, 9986–9995 (2021).
2. Wang, S. Y. et al. Nitrogen fixation reaction derived from nanostructured catalytic materials. *Adv. Funct. Mater.* **28**, 1803309 (2018).
3. Xin, Y. et al. Atomic-level insights into the activation of nitrogen via hydrogen-bond interaction toward nitrogen photofixation. *Chem* **7**, 1–19 (2021).
4. Yang, J. H. & Yu, J. C. Photodriven disproportionation of nitrogen and its change to reductive nitrogen photofixation. *Angew. Chem., Int. Ed.* **133**, 940 (2021).
5. Ran, Y. & Ye, J. H. Polymeric carbon nitride with frustrated Lewis pair sites for enhanced photofixation of nitrogen. *J. Mater. Chem. A*, **8**, 13292–13298 (2020).
6. Li, H. & Zhang, L. Z. Efficient visible light nitrogen fixation with BiOBr nanosheets of oxygen vacancies on the exposed {001} facets. *J. Am. Chem. Soc.* **137**, 6393–6399 (2015).
7. Bo, Y. N. & Xiong, Y. J. Altering hydrogenation pathways in photocatalytic nitrogen fixation by tuning local electronic structure of oxygen vacancy with dopant. *Angew. Chem. Int. Ed.* doi: **10.1002/ange.202104001**.
8. Yang, J. H. & Yu, J. C. High-Efficiency “Working-in-Tandem” Nitrogen Photofixation achieved by assembling plasmonic gold nanocrystals on ultrathin titania nanosheets. *J. Am. Chem. Soc.* **140**, 8497–8508 (2018).
9. Zhang, Y. D. et al. Dual-metal sites boosting polarization of nitrogen molecules for efficient nitrogen photofixation. *Adv. Sci.* **8**, 2100302 (2021).
10. Liu, X. F. et al. Rare earth La single atoms supported  $\text{MoO}_{3-x}$  for efficient photocatalytic nitrogen fixation. *Appl. Catal., B* **301**, 120766 (2022).
11. Yuan, J. L. et al. Efficient photocatalytic nitrogen fixation: enhanced polarization, activation, and cleavage by asymmetrical electron donation to  $\text{N} \equiv \text{N}$  bond. *Adv. Funct. Mater.* **30**, 1906983 (2020).
12. LÉGARÉ, M.-A. et al. Nitrogen fixation and reduction at boron. *Science*, **359**, 896 (2018).
13. Tanaka, H. et al. Interplay between theory and experiment for ammonia synthesis catalyzed by transition metal complexes. *J. Am. Chem. Soc.* **139**, 12480–12487 (2017).
14. Ortel, E. et al. Supported mesoporous and hierarchical porous Pd/TiO<sub>2</sub> catalytic coatings with controlled particle size and pore structure. *Chem. Mater.* **24**, 3828–3838 (2012).
15. Li, J. et al. Oxygen vacancies on TiO<sub>2</sub> promoted the activity and stability of supported Pd nanoparticles for the oxygen reduction reaction. *J. Mater. Chem. A* **6**, 2264–2272 (2018).
16. Li, N. X. et al. Enhanced photocatalytic performance toward CO<sub>2</sub> hydrogenation over nanosized TiO<sub>2</sub> loaded Pd under UV irradiation. *J. Phys. Chem. C* **121**, 2923–2932 (2017).

17. Xu, C. Y. et al. Photothermal coupling factor achieving CO<sub>2</sub> reduction based on palladium-nanoparticle-loaded TiO<sub>2</sub>. *ACS Catal.* **8**, 6582–6593 (2018).
18. Di, J. et al. Defect-tailoring mediated electron–hole separation in single-unit-cell Bi<sub>3</sub>O<sub>4</sub>Br nanosheets for boosting photocatalytic hydrogen evolution and nitrogen fixation. *Adv. Mater.* **31**, 1807576 (2019).
19. Zhang, R. H. et al. Photocatalytic oxidative dehydrogenation of ethane using CO<sub>2</sub> as a soft oxidant over Pd/TiO<sub>2</sub> catalysts to C<sub>2</sub>H<sub>4</sub> and syngas. *ACS Catal.* **8**, 9280–9286 (2018).
20. Zhang, C. B. et al. Sodium-promoted Pd/TiO<sub>2</sub> for catalytic oxidation of formaldehyde at ambient temperature. *Environ. Sci. Technol.* **48**, 10, 5816–5822 (2014).
21. Guo, W. et al. Pd nanoclusters/TiO<sub>2</sub>(B) nanosheets with surface defects toward rapid photocatalytic dehalogenation of polyhalogenated biphenyls under visible light. *Appl. Catal., B* **277**, 119255 (2020).
22. Raza, F.Z. et al. Structuring Pd nanoparticles on 2H-WS<sub>2</sub> nanosheets induces excellent photocatalytic activity for cross-coupling reactions under visible light, *J. Am. Chem. Soc.* **139**, 1467–14774 (2017).
23. Yang, S. et al. Synthesis of titanium dioxide with oxygen vacancy and its visible-light sensitive photocatalytic activity. *Mater. Res. Bull.* **46**, 531–537 (2011).
24. Saknarin C. et al. Impact of oxygen vacancy on the photocatalytic selective hydrogenation of 3-Nitrostyrene via calcination of TiO<sub>2</sub>. *Mater. Sci. Eng.* **559**, 012015 (2019).
25. Yu, K. et al. Asymmetric oxygen vacancies: the intrinsic redox active sites in metal oxide catalysts. *Adv. Sci.* **7**, 2, 1901970 (2019).
26. Peter R. Fundamentals and engineering of defects. *Prog. Cryst. Growth Charact. Mater.* **62**, 2, 89–110 (2016).
27. Liu, P. X. et al. Photochemical route for synthesizing atomically dispersed palladium catalysts. *Science* **352**, 797–800 (2016).
28. Kuai, L., Chen, Z., Liu, S. et al. Titania supported synergistic palladium single atoms and nanoparticles for room temperature ketone and aldehydes hydrogenation. *Nat. Commun.* **11**, 48 (2020).
29. Zhou, W. J. et al. PdO/TiO<sub>2</sub> and Pd/TiO<sub>2</sub> Heterostructured nanobelts with enhanced photocatalytic activity. *Chem. Asian J.* **9**, 1648–1654 (2014).
30. Espino-Estévez, M. R. et al. Effect of TiO<sub>2</sub>–Pd and TiO<sub>2</sub>–Ag on the photocatalytic oxidation of diclofenac, isoproturon and phenol. *Chem. Eng. J.* **298**, 82–95 (2016).
31. Zhang, N. et al. Synthesis of M@TiO<sub>2</sub> (M = Au, Pd, Pt) core–shell nanocomposites with tunable photoreactivity. *J. Phys. Chem. C* **115**, 9139–9145 (2011).
32. Zou, N. M. et al. Imaging catalytic hotspots on single plasmonic nanostructures via correlated super-resolution and electron microscopy. *ACS Nano* **12**, 5570–5579 (2018).
33. Ma, X. C. et al. Energy transfer in plasmonic photocatalytic composites. *Light Sci. Appl.* **5**, e16017 (2016).

34. Liu, X. et al. Noble metal – metal oxide nanohybrids with tailored nanostructures for efficient solar energy conversion, photocatalysis and environmental remediation. *Energy Environ. Sci.* **10**, 402–434 (2017).
35. Jiang, R. et al. Metal/semiconductor hybrid nanostructures for plasmon-enhanced applications. *Adv. Mater.* **26**, 5274 – 5309 (2014).
36. Chen, Y. et al. Enhancement of photocatalytic performance with the use of noble-metal-decorated TiO<sub>2</sub> nanocrystals as highly active catalysts for aerobic oxidation under visible-light irradiation. *Appl. Catal., B* **210**, 352–367 (2017).
37. Pan, X. Y. & Xu, Y.-J. Defect-mediated growth of noble-metal (Ag, Pt, and Pd) nanoparticles on TiO<sub>2</sub> with oxygen vacancies for photocatalytic redox reactions under visible light. *J. Phys. Chem. C* **117**, 35, 17996–18005 (2013).
38. Pan, C.-J. et al. Tuning/exploiting strong metal-support interaction (SMSI) in heterogeneous catalysis. *J. Taiwan Inst. Chem. E.* **74**, 154–186 (2017).
39. Knight, M. W. et al. Embedding plasmonic nanostructure diodes enhances hot electron emission. *Nano Lett.* **13**, 1687–1692 (2013).
40. Bolleter, W. T. et al. Spectrophotometric determination of ammonia as indophenol. *Anal. Chem.* **33**, 4, 592–594 (1961).
41. Dong, G. H. et al. Selective photocatalytic N<sub>2</sub> fixation dependent on g-C<sub>3</sub>N<sub>4</sub> induced by nitrogen vacancies. *J. Mater. Chem. A* **3**, 23435–23441 (2015).
42. Zhang, S. et al. Efficient Photocatalytic Nitrogen Fixation over Cu<sup>δ+</sup>-Modified Defective ZnAl-layered double hydroxide nanosheets. *Adv. Energy Mater.* **10**, 1901973 (2019).
43. Li P. S. et al. Visible-light-driven nitrogen fixation catalyzed by Bi<sub>5</sub>O<sub>7</sub>Br nanostructures: Enhanced performance by oxygen vacancies. *J. Am. Chem. Soc.* **142**, 12430–12439 (2020).
44. Zhang, N. et al. Refining defect states in W<sub>18</sub>O<sub>49</sub> by Mo doping: A strategy for tuning N<sub>2</sub> activation towards solar-driven nitrogen fixation. *J. Am. Chem. Soc.* **140**, 9434–9443 (2018).
45. Sun, Y. et al. Pits confined in ultrathin cerium(IV) oxide for studying catalytic centers in carbon monoxide oxidation. *Nat. Commun.* **4**, 2899 (2013).
46. Liu, Y. et al. Carbon-nanoplated CoS@TiO<sub>2</sub> nanofibrous membrane: an interface-engineered heterojunction for high-efficiency electrocatalytic nitrogen reduction. *Angew. Chem. Int. Ed.* **58**, 18903–18907 (2019).
47. Lv, C. D. et al. An amorphous noble-metal-free electrocatalyst that enables nitrogen fixation under ambient conditions. *Angew. Chem. Int. Ed.* **57**, 6073 – 6076 (2018).
48. Cai, Y. T. et al. Soft BiOBr@TiO<sub>2</sub> nanofibrous membranes with hierarchical heterostructures as efficient and recyclable visible-light photocatalysts. *Environ. Sci.: Nano* **5**, 2631–2640 (2018).
49. Xue, J. J. et al. Electrospinning and electrospun nanofibers: methods, materials, and applications. *Chem. Rev.* **119**, 5298–5415 (2019).

50. Li, D. & Xia, Y. N. Fabrication of titania nanofibers by electrospinning. *Nano Lett.* **3**, 4, 555–560 (2003).

## Figures

### Figure 1

**a** Schematic Illustration of fabrication procedure for se-Pd/m-TiO<sub>2</sub> NRs photocatalyst. **b** HRTEM imaging of the m-TiO<sub>2</sub> NRs. **c** TEM image of the as-prepared se-Pd/m-TiO<sub>2</sub> NRs; Inset: The particle size distribution of se-Pd NPs on m-TiO<sub>2</sub> NRs. **d** HRTEM imaging of the as-prepared se-Pd/m-TiO<sub>2</sub> NRs; The inset graph in panel (**d**) shows se-Pd NPs. **e** Scanning TEM imaging and (**f-h**) EDS elemental mapping of the as-prepared se-Pd/m-TiO<sub>2</sub> NRs.

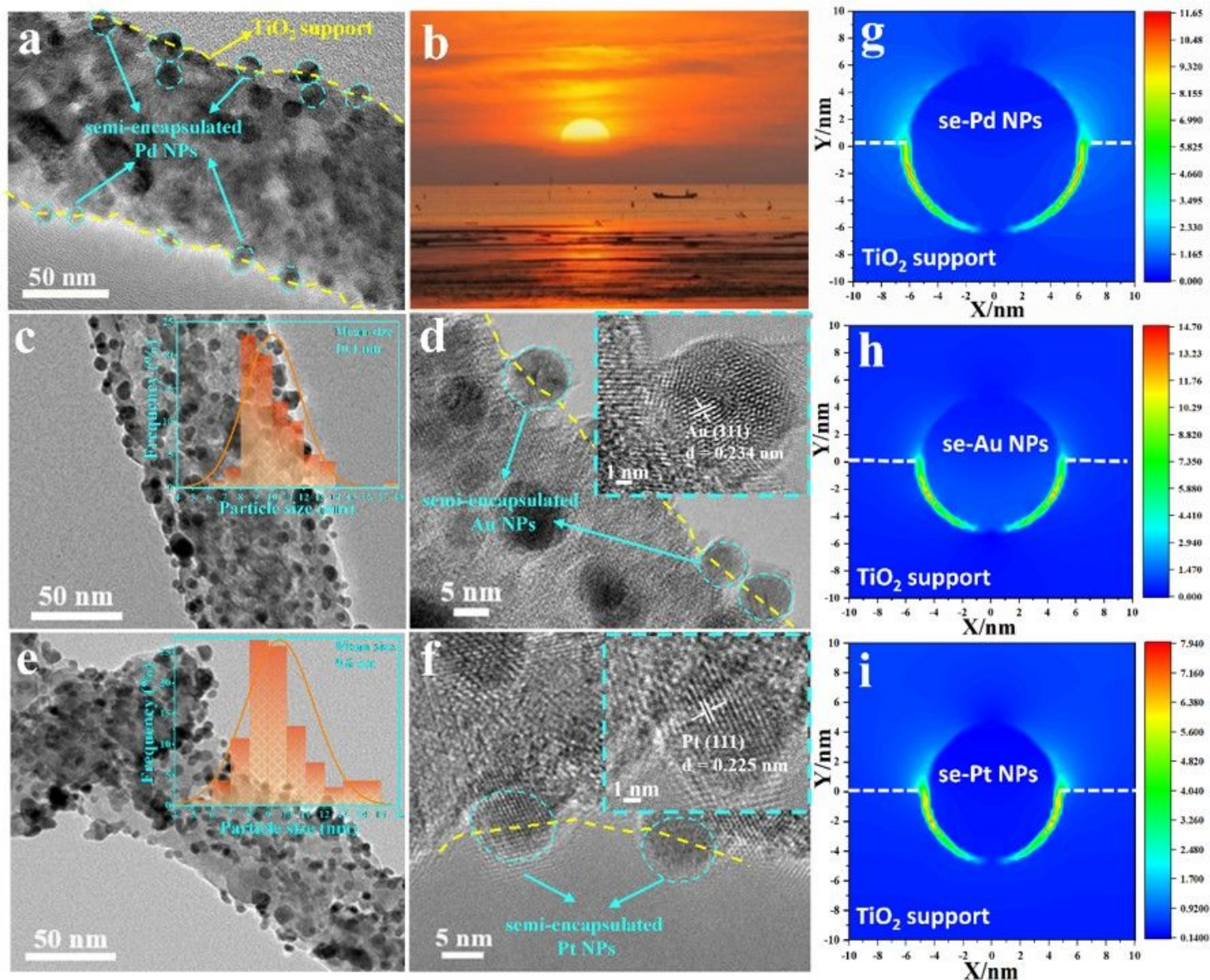


**Figure 2**

**a** TEM image of se-Pd/m-TiO<sub>2</sub> NRs. **b** Scenery described in ancient Chinese poetry (The structure model of se-Pd/m-TiO<sub>2</sub> NRs catalyst resembles a scene described in a Chinese classical poem when the sun goes down halfway). TEM images of se-Au/m-TiO<sub>2</sub> NRs (**c**), and se-Pt/m-TiO<sub>2</sub> NRs (**e**); the insets of (**c**) and (**e**) are the particle size distribution of se-Au and Pt NPs. HRTEM images of se-Au/m-TiO<sub>2</sub> NRs (**d**) and se-Pt/m-TiO<sub>2</sub> NRs (**f**). Spatial distribution of the LSPR-induced enhancement of the electric field intensity from the FDTD simulations for the se-Pd/m-TiO<sub>2</sub> NRs (**g**), se-Au/m-TiO<sub>2</sub> NRs (**h**) and se-Pt/m-TiO<sub>2</sub> NRs (**i**) at the excitation wavelengths of 550 nm.

**Figure 3**

High-resolution **a** Ti 2p, **b** O 1s and **c** Pd 3d XPS spectra for m-TiO<sub>2</sub> NRs and se-Pd/m-TiO<sub>2</sub> NRs. **d** EPR spectra of m-TiO<sub>2</sub> NRs and se-Pd/m-TiO<sub>2</sub> NRs. **e** Spectra of XANES for Pd K-edge. **f** The  $k^3$ -weighted Fourier transforms of Pd K-edge EXAFS spectra, and **g** the wavelet transforms from experimental outcomes for se-Pd/m-TiO<sub>2</sub> NRs, PdO, and Pd foil.

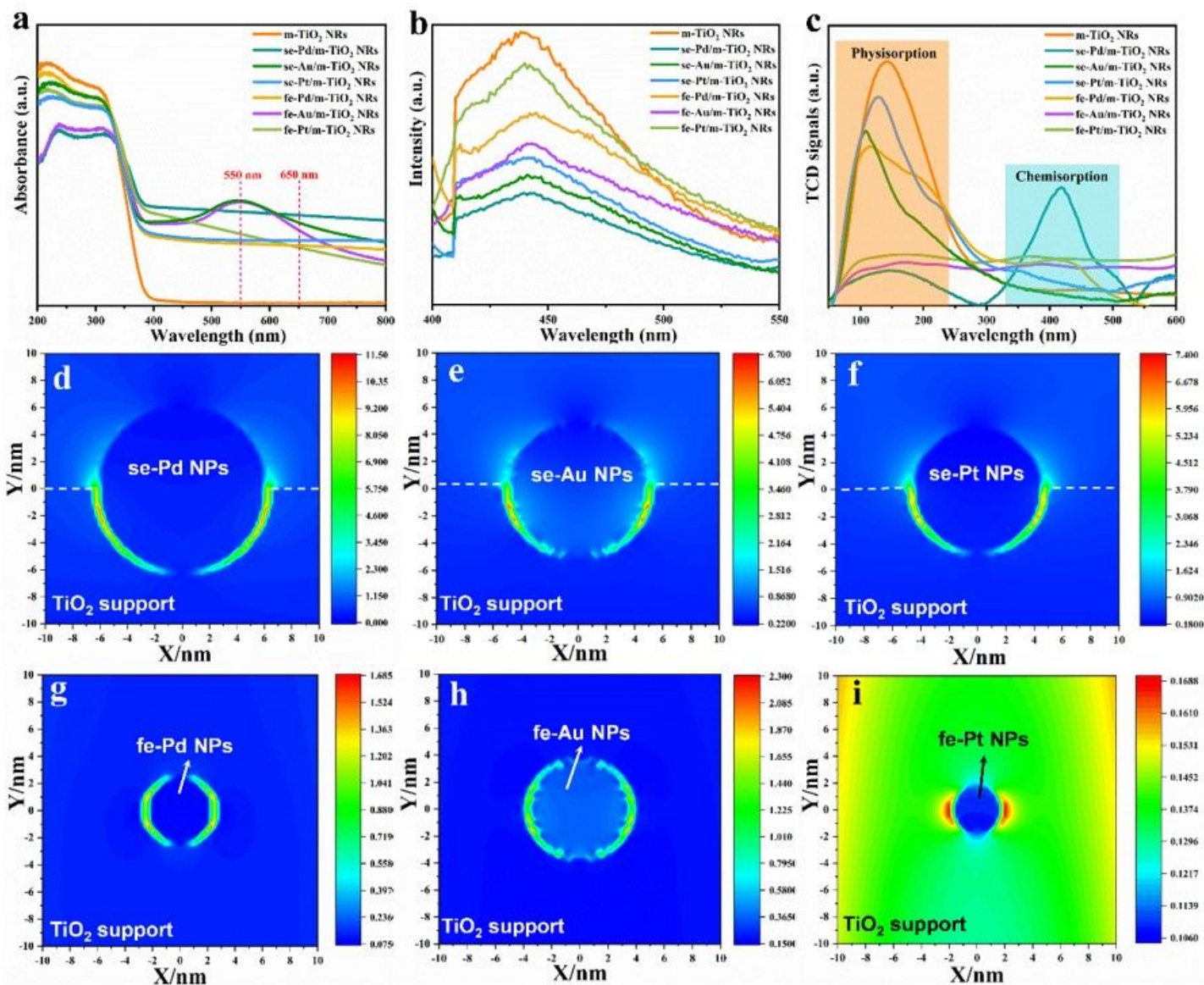


**Figure 4**

**a** Spectra of UV-vis DRS, **b** Steady-state PL spectra and **c** N<sub>2</sub>-TPD spectra of the as-constructed various photocatalysts. Spatial distribution of the LSPR-induced enhancement of the electric field intensity from the FDTD simulations for the se-Pd/m-TiO<sub>2</sub> NRs (**d**), se-Au/m-TiO<sub>2</sub> NRs (**e**), se-Pt/m-TiO<sub>2</sub> NRs, (**f**) fe-Pd/m-TiO<sub>2</sub> NRs (**g**), fe-Au/m-TiO<sub>2</sub> NRs (**h**) and the fe-Pt/m-TiO<sub>2</sub> NRs (**i**) at excitation wavelengths of 650 nm.

## Figure 5

**a** Photocatalytic  $\text{NH}_3$  production rates for m-TiO<sub>2</sub> NRs, se-Pd/m-TiO<sub>2</sub> NRs, se-Au/m-TiO<sub>2</sub> NRs, se-Pt/m-TiO<sub>2</sub> NRs, fe-Pd/m-TiO<sub>2</sub> NRs, fe-Au/m-TiO<sub>2</sub> NRs and fe-Pt/m-TiO<sub>2</sub> NRs in N<sub>2</sub>-saturated water under light irradiation. **b**  $\text{NH}_3$  synthesis rates of se-Pd/m-TiO<sub>2</sub> NRs in different contrast conditions. **c** Cycling tests of se-Pd/m-TiO<sub>2</sub> NRs. (The reaction was tested for 3 h in each cycle, and the performance of the first 1 h of reaction was taken as reference). **d** *In situ* FTIR spectra collected from se-Pd/m-TiO<sub>2</sub> NRs during photocatalytic N<sub>2</sub> fixation.

## Figure 6

The optimized adsorption configuration of N<sub>2</sub> molecule on Ti sites of TiO<sub>2</sub> (101) surface, Pd (111), OVs in TiO<sub>2</sub> (101)/Pd (111) and Ti-N<sub>2</sub>-Pd dual sites at the TiO<sub>2</sub> (101)/Pd (111) interface.

## Figure 7

The number of electrons transferred to N<sub>2</sub> molecules on (a) N<sub>2</sub>-TiO<sub>2</sub> (101), (b) N<sub>2</sub>-OVs-TiO<sub>2</sub> (101), (c) N<sub>2</sub>-Pd (111) and Ti-N<sub>2</sub>-Pd interface model are illustrated by first-principles simulations.

## Figure 8

DFT calculations: **a** Adsorption energies of N<sub>2</sub> on single Ti site of TiO<sub>2</sub> (101), Pd sites, OVs of TiO<sub>2</sub> (101)/Pd (111), and on Ti-Pd dual sites at TiO<sub>2</sub> (101)/Pd (111) interface. **b** Differential charge density of TiO<sub>2</sub> (101)-N<sub>2</sub>-Pd (111) interface (yellow and orange red colors illustrate an enhancement and reduction in electron density, accordingly). **c** N-N distance of free N<sub>2</sub>, \*NN on TiO<sub>2</sub> (101), Pd (111), OVs in TiO<sub>2</sub> (101) and the interface between TiO<sub>2</sub> (101)/Pd (111) model. **d** Distances of N-N for free N<sub>2</sub> and intermediates during hydrogenation beginning from the N on Ti or Pd. **e** Gibbs free energy diagrams of N<sub>2</sub> photoreduction to NH<sub>3</sub> through different paths over the TiO<sub>2</sub> (101)/Pd (111) interface (blue line represents the optimal pNRR process, gray line represents other possibilities of pNRR paths); The insets are optimized atomic structure models of N<sub>2</sub> adsorption and reduction on the Ti-Pd dual sites of TiO<sub>2</sub>

(101)/Pd (111) interface (Color code: gray, red, dark cyan, blue, and green are Ti, O, Pd, N, and H atoms, respectively; asterisk for activated site).

## Supplementary Files

This is a list of supplementary files associated with this preprint. Click to download.

- [SupplementaryInformation.docx](#)